Characterization of wurtzite $Zn_{1-x}Mg_xO$ epilayers grown on $ScAlMgO_4$ substrate by methods of optical spectroscopy

Laima Trinkler[1], Ilze Aulika[1], Guna Krieke[1], Dace Nilova[1], Rihards Ruska[1], Jelena Butikova[1], Baiba Berzina[1], Mitch Ming-Chi Chou[2,3], Liuwen Chang[2,3], Meng-Chieh Wen[2,3], Tao Yan[4], Ramunas Nedzinskas[5]

[1] *Institute of Solid State Physics, University of Latvia, Kengaraga St.8, Riga LV-1063, Latvia*
[2] *Department of Materials and Optoelectronic Science, National Sun Yat-sen University, Kaohsiung 80424, Taiwan*
[3] *Center of Crystal Research, National Sun Yat-sen University, Kaohsiung 80424, Taiwan*
[4] *Key Laboratory of Optoelectronic Materials Chemistry and Physics, Fujian Institute of Research on the Structure of Matter, Chinese Academy of Sciences, Fuzhou, People's Republic of China*
[5] *Center for Physical Sciences and Technology, Vilnius, Saulėtekio ave. 3, Vilnius 10257, Lithuania*

Abstract

Wurtzite $Zn_{1-x}Mg_xO$ epilayers (x=0, 0.26, 0.44, 0.49, 0.66) grown by the plasma-assisted molecular beam epitaxy on $ScAlMgO_4$ substrate were characterized using the methods of optical spectroscopy: spectroscopic ellipsometry (SE), optical absorption (OA), and photoluminescence (PL). The complex dielectric function in the spectral range of 210 to 1690 nm, band gap width, exciton absorption and emission parameters, and film quality were studied and discussed. Individual characterization of samples was provided by combining SE and OA measurement results. The observed increase of the band gap up to 4.35 eV with the rise of the MgO content allowed the recommendation of the wurtzite $Zn_{1-x}Mg_xO$ epilayers as material for UV sensors. The origin of defects hampering the practical application of the materials was discussed.

Keywords: $Zn_{1-x}Mg_xO$ thin films; optical properties; optical spectroscopy; light absorption; luminescence; composition fluctuations.

1. Introduction

Zinc oxide ZnO has found numerous applications due to its unique properties: thermal and chemical stability, low density of defects, and strong radiation hardness, which determine a wide range of applications such as LEDs, sensors, catalysts, photodetectors, solar cells, and thermoelectric devices. Different chemical and physical methods have been used to produce high-quality ZnO structures. The aspects of morphology, preparation method, modification, doping, and the composite of ZnO–based material for the mentioned applications have been discussed in recent reviews [1-14]. ZnO antibacterial properties for disinfection, supplementation, and immunomodulation applications also have been studied [15-17]. Besides, ZnO nanostructures have been studied as the transducer elements in different types of PL-based biosensors for the detection of analytes relevant to health and the environment, like antibiotics, glucose, bacteria, and virus or tumor biomarkers [18, 19]. ZnO-based engineered nanomembranes, nanocomposites and nanoparticles have been used in water purification technologies [20, 21]. In combination with MgO, zinc oxide demonstrates excellent ferroelectric and piezoelectric properties, beneficial for practical application [22, 23] and large non-linear susceptibility, enabling ultrafast nonlinear optical devices [24].

ZnO has attracted great interest as a material prospective for electronic and optoelectronic applications in the ultraviolet range [25, 26] due to the advantageous properties: direct wide band gap (3.37 eV at 4 K; 3.3 at RT) [1, 2, 27, 28] and large free exciton binding energy (60 meV) [28], providing exciton emission at and above room temperatures.

Even more possibilities for application in the deep ultraviolet region (< 300 nm) may be expected from ZnO compounds combining it with some elements from groups II and III, such as Be, Mg, Ca [29, 30]. Furthermore, variations in components' mutual concentration allow for tuning of the compound band gap in a controllable way. Deep UV photon sensors based on ZnO-related compounds can be used as biological and chemical sensors for ozone detection and as detectors for water purification, as well as sensors for detection of pollution levels in any biological agent [31]. Up to now, the most prospective ZnO combinations were reported with the use of MgO (direct band gap with E_g = 7.8 eV [32-34]), producing alloy thin films and heterostructures with different techniques (PLD, MOCVD, magnetron sputtering, plasma-assisted MBE, etc.), using different substrates (ZnO, sapphire or quartz wafers, SiO_2, and others) [35, 36 and references therein] and different buffer layers. Thus, *a*-plane MgZnO films were grown on a-GaN/r-sapphire by PLD [37], ZnMgO thin films were produced by plasma-assisted MBE on *c*-plane sapphire substrates using MgO/ZnMgO buffer layer [38]. The same method was used in combination with ZnO substrate and ZnO buffer layer [39], ZnMgO monocrystalline thin films were produced on glass and silicon substrate by E-beam deposition technique [40], ZnO/$Zn_{1-x}Mg_xO$ multiple quantum wells were grown on $LiGaO_2$ substrate using plasma-assisted MBE [41], high-quality ZnMgO thin films were grown on Zn-O seed-layer-coated oxide glass substrates using the electrochemical deposition [42], etc. Potentially $Zn_{1-x}Mg_xO$ compounds may provide a tunable band gap in the 3.3-7.8 eV range, which covers the deep UV region of the highest interest. Promising results in achieving band gap engineering (E_g = 4.5...5.7 eV) were obtained for $Zn_{1-x}Mg_xO$ single quantum wells with Mg content x = 0.2 … 0.8 grown by molecular beam epitaxy technique [34].

In general, alloying ZnO and MgO into the $Zn_{1-x}Mg_xO$ compound is challenging. Due to different crystal structures, mutual solubility of ZnO (non-centrosymmetric hexagonal wurtzite (WZ) lattice structure) and MgO (rock salt (RS) lattice structure) has certain limits, beyond which phase separation occurs, preventing achieving compounds with a band gap in the 4.3-5.5 eV range. However, this obstacle can be overcome by stabilizing the crystal structure of binary compounds by using low lattice mismatch substrates with a hexagonal structure such as $ScAlMgO_4$ (SCAM) for the high MgO-content WZ $Zn_{1-x}Mg_xO$; and cubic MgO or Cu_2O substrates for high ZnO-content RS $Zn_{1-x}Mg_xO$ epilayers. This concept was implemented by Wen et al., using the MBE method to successfully produce rock-salt $Zn_{1-x}Mg_xO$ epilayers with x=0.22-0.87 on MgO substrate [43] and wurtzite $Zn_{1-x}Mg_xO$ epilayers with x=0.26-0.66 on SCAM substrate [44]. Both types of ZnMgO thin films demonstrated a blue shift of the band gap value with increasing MgO content. The highest Mg content reported in WZ ZnMgO by PA MBE was 74.6 %, with the estimated band gap of 5.9 eV [45]; however, the PL of the sample contained a strong emission band from pure ZnO, confirming the inhomogeneity of the compound.

The present paper focuses on the characterization of the WZ $Zn_{1-x}Mg_xO$ (x= 0,…, 0.66) thin layers grown on SCAM substrate with the MBE method, using the methods

of spectroscopic ellipsometry (SE), optical absorption (OA), and photoluminescence (PL). The main attention is focused on the detection of the band gap, which is the most important parameter for application of these materials for deep UV sensors. The task of the present study is to evaluate the applicability of the WZ $Zn_{1-x}Mg_xO$ compounds with a tuned band gap for deep UV sensors.

2. Experimental

2.1. Samples

Hexagonal WZ $Zn_{1-x}Mg_xO$ epilayers were deposited on (0001) $ScAlMgO_4$ substrates by plasma-assisted molecular beam epitaxy (PA-MBE). Prior to the epitaxial growth, the substrate in size of 10x10 mm^2 was annealed at 1000 ^oC for one day, subsequently followed by cleaning in acetone and isopropanol. Detailed growth conditions were described in a previously published paper [44]. Both pure ZnO epilayer and pseudobinary epilayers $Zn_{1-x}Mg_xO$ with x=0.26-0.66 were grown and characterized by X-ray diffraction and cathodoluminescence methods and reported by Wen et al. [44]. X-ray diffraction showed that only the sample with the largest amount of MgO content (66%) had a minor contribution of the RS phase, while all other samples possessed only the WZ structure. MgO compositions in the ready $Zn_{1-x}Mg_xO$ samples were determined by the energy-dispersive X-ray spectroscopy (EDS) method. The thickness of the $Zn_{1-x}Mg_xO$ layer varied in the 100-300 nm range depending on the used ZnO and MgO fluxes.

2.2. Methods and Equipment

In the present research, the samples were studied by methods of spectroscopic ellipsometry (SE), optical absorption (OA), and photoluminescence (PL).

Spectroscopic ellipsometry. Optical properties and film thicknesses were obtained employing spectroscopic ellipsometer (SE) WOOLLAM RC2 in the spectral range from 210 to 1690 nm (or from 5.9 to 0.7 eV). The main ellipsometric parameters Ψ and Δ were measured at the incident angles from (55-70)° with the 5° step. Refractive index *n* and extinction coefficient *k* dispersion curves were modelled using Gaussian (GO) and Tauc-Lorentz oscillator (TLO) functions [45]. The optical properties of the SCAM were obtained from SE measurements of pure substrates without films. The surface roughness was modelled utilizing Bruggeman effective medium approximation (EMA) [46]. The optical gradient of *n* and *k* was calculated by dividing the film layer into sub-layers with smaller thicknesses and applying the EMA, considering the films as a mixture of voids to vary the *n* and *k* values from the bottom to the top of the film [47]. SE experimental data model-based regression analyses were performed with the WOOLLAM software CompleteEASE®. The substrate and films were modelled as isotropic materials despite the WZ and RS crystallographic orientation of the SCAM and $Zn_{1-x}Mg_xO$ because the anisotropic measurements had shown that the off-diagonal Muller matrix (MM) elements were near zero and not changing with the azimuthal sample orientation respect to the SE coordinate system. The $Zn_{1-x}Mg_xO$ films were too thin to distinguish different optical paths due to film anisotropy. Nevertheless, the reflectance MM measurements showed no anisotropy presence for current SCAM substrates and thin films, thus, permitting to neglect anisotropy and to model the substrate and the films as isotropic materials.

Optical absorption and photoluminescence. OA was measured using the UV VIS spectrophotometer Specord 210 (Analytik Jena AG). The samples were inserted in the closed cycle helium refrigerator (Janis), providing sample temperature of 10-300 K, which, in turn, was embedded in the spectrophotometer sample compartment. PL was excited with the wavelength-tunable pulsed solid-state laser Ekspla NT342/3UV as an excitation source and detected with the Andor Kymera 328i-B2 spectrometer coupled with the Andor iStar sCMOS CCD camera. PL spectra of $Zn_{1-x}Mg_xO$ samples were measured under excitation light at 260 nm, while those of ZnO sample - at 290 nm excitation. These excitation wavelengths were chosen as optimal, taking into account excitation efficiency and spectral separation from emission bands of the $Zn_{1-x}Mg_xO$ samples, peaking in the 290-330 nm region for x = 0.26, …, 0.66 and at 373 nm for x = 0. For the PL measurements, the samples were cooled using an Advanced Research Systems DE202 N closed-cycle helium refrigerator in the 10-300 K temperature range.

3. Results and discussion

3.1. Spectroscopic Ellipsometry

SE is a powerful method for sensing very thin layers. Many commercially available SE instruments measure the main ellipsometric angles (Ψ, Δ) with a resolution of 0.001°; thus, SE can measure the sub-angstrom thickness change [48] and detect the presence of a very small amount of substances.

In ellipsometry, the two main ellipsometric angles (Ψ, Δ), which are functions of wavelength λ and incident angle of light θ, are defined by

$$\rho \equiv \tan(\Psi)e^{i\Delta} = \frac{|\widetilde{r_p}|}{|\tilde{r}_s|} = \frac{E_p^{out}/E_p^{in}}{E_s^{out}/E_s^{in}} \quad (1),$$

where $\tilde{r}_p$ and $\tilde{r}_s$ are Fresnel's coefficients for *p* (parallel) and *s* (perpendicular) polarized light, $E_p^{out}, E_p^{in}, E_s^{out},$ and E_s^{in} represent *p* and *s* components of the incident and reflected electric fields of the light beam [49 Zubkins]. TanΨ is the amplitude ratio upon reflection and $\Delta = \delta_p - \delta_s$ is the phase shift induced by the reflection between the *p*-wave and the *s*-wave. The ratio ρ is related to the optical properties of the material or materials under investigation, namely, the complex refractive index $\widetilde{N} = n + ik$, where *n* is the index of refraction and *k* - extinction coefficient. The high sensitivity of this technique is derived from the fact that the detected (Ψ, Δ) is a relative measurement of the change in polarization (a ratio or difference of two values rather than the absolute value of either), which explains robustness, high accuracy, and reproducibility of the technique.

Experimental and modelled main ellipsometric angles Ψ and Δ as a function of incident angle θ and photo energy *E* are presented in Figure 1 for the $Zn_{0.74}Mg_{0.26}O$ epilayer, which was taken as an example. The low oscillation of (Ψ, Δ) in the VIS and NIR spectral range (0.7 - 3 eV) could be explained by the similarity of refractive indexes *n* of SCAM substrate and $Zn_{1-x}Mg_xO$ thin films (Fig. 2). The larger is the difference between (*n*, *k*) of the substrate and the film, the larger are the (Ψ, Δ) oscillations. For example, the Ψ and Δ oscillations could reach up to 20° and 350° for ZnO thin films on a glass substrate [49], and up to 10° and 40° on Pt substrate [50]. The low oscillations in (Ψ, Δ) cause larger errors in the fitting parameters, especially in the case of the presence of optical gradient, and proper model development becomes much more challenging and time-consuming.

The modelled isotropic dispersion curves have shown that with an increase of MgO content, the peak positions of the (*n*, *k*) curves and optical band gap E_g (fitting parameter of the Tauc-Lorentz oscillator) shifted towards higher *E* values (Fig. 2). At low *E* in the range of ~ 0.7-1.8 eV, refractive index values for all measured $Zn_{1-x}Mg_xO$ samples with $x \neq 0$ were higher with respect to pure ZnO thin film (Fig. 2a). The decrease of *n* from 1.88 to 1.75 at low photon energies was observed for $Zn_{1-x}Mg_xO$ epilayers with the increase of MgO content from 0.26 to 0.66, which was related to the lattice disorder. Despite the small difference in ionic radii of Zn^{2+} and Mg^{2+}, replacing Zn^{2+} with Mg^{2+} distorted the cation tetrahedrons and decreased the lattice constants ratio c/a of the wurtzite ZMO. These distortions were attributed to the changes in the electronic configuration of the two cations, which resulted in the decrease of refractive index and blue shift of the E_g in the WZ ZMO compounds [51]. Obtained results were in good agreement with the experimental [52, 53] and theoretical reports [54].

SE analysis showed that all films exhibited some imperfections: (1) surface roughness from 4 nm up to 34 nm, (2) optical gradient for $Zn_{0.34}Mg_{0.66}O$ (Fig. 3), (3) thickness non-uniformity (confirmed by TEM) for ZnO and $Zn_{0.34}Mg_{0.66}O$ thin films, and (4) the presence of the interphase (confirmed by TEM) between the substrate and the film with the thickness of 7 nm for $Zn_{0.51}Mg_{0.49}O$ (ZnO buffer) and 14 nm for $Zn_{0.74}Mg_{0.26}O$ (ZnO buffer) thin films. The surface roughness tended to increase with the increase of MgO content in the films. The presence of the interphase was related to a thin ZnO buffer layer of ~5 nm deposited at 700 °C prior to the epitaxial growth of ZMO [44]. Indeed, the optical properties of the modelled interphase layer were comparable with those of ZnO thin film. The presence of the thicker interphase layer (14 nm) might be related to the fact that the first layers of ZMO had optical properties similar to ZnO and in the model, it was considered an interphase.

The best model fit for $Zn_{0.34}Mg_{0.66}O$ was found by considering the sample as a two-layer film to perform complicated refractive index variation within the film depth (see curves (5') and (5") in Figure 2). The CompleteEASE software permitted continuous optical gradient modelling within one layer film, which in the case of $Zn_{0.34}Mg_{0.66}O$ gave mean square error (MSE) up to 20, which was a rather high value for SE. Good model fit in SE gives MSE only up to 3. The presence of high and asymmetric amplitudes of Ψ for $Zn_{0.34}Mg_{0.66}O$ compelled the consideration of sharp refractive index changes within the film, which could be modelled with CompleteEASE only if the film was considered as a two-layer model, even if physically, the film was made of one layer. The anisotropic and backside reflection effects on (Ψ, Δ) spectra of $Zn_{0.34}Mg_{0.66}O$ were excluded since Muller Matrix off-diagonal elements showed to be near zero, and no depolarization was observed in the visible spectral range.

Both layers, which described $Zn_{0.34}Mg_{0.66}O$ thin film, exhibited optical gradient (Fig. 3, curves (2') and (2")): *n* drastically decreased the thickness of layer 1 from ~60 nm up to ~80 nm and then reached values of the second layer; the layer 2 had slight gradient near the surface from ~220 nm to 260 nm thickness. Layer 2 showed smaller changes in refractive index with the thickness increase compared to layer 1. The presence of such a complex optical gradient might be related to some irregularity of the film deposition process (e.g., slight, very short-term variation in ZnO and MgO fluxes). The optical properties of layer 1 were comparable with the ZnO thin film in

terms of E_g. The refractive index for layer 1 was found to be lower compared to the ZnO thin film. Considering the previous studies on ZnO [49, 50] and information available in the literature [55], the obtained *n* values for the interphase layers, layer 1 of $Zn_{0.34}Mg_{0.66}O$ and Zn_1Mg_0O were found to be comparable to *n* values of an amorphous ZnO thin film. Based on TEM observation, a ~20 nm thin ZnO layer was determined between ZMO and SCAM. For some ZMO thin films, this thin interphase layer was also detected by SE (see interphase layer thickness in Table 1). For all ZnO-MgO thin films, the low *n* values were related to the structural fluctuations resulting in lower density seen as reduced *n* values of these films.

The thickness of the interphase d_{int}, the thickness of the epilayer *d* (roughness excluded), the thickness of non-uniformity d_{NU} (%), the surface roughness d_s (nm), the optical band gap E_g and refractive index *n* at 632.8 nm (HeNe laser wavelength) obtained from SE for five $Zn_{1-x}Mg_xO$ compounds were summarized in Table 1. The high error for E_g of $Zn_{0.56}Mg_{0.44}O$ was due to very small oscillations of (Ψ, Δ) related to similar optical constants between SCAM and this thin film, thus, reducing the sensitivity of the SE method.

Table 1. Optical properties of $Zn_{1-x}Mg_xO$ compounds obtained from SE measurements.

$Zn_{1-x}Mg_xO$	MSE	d_{int}, nm	*d* by SE, nm	d_{NU}, %	d_s, nm	*d* by TEM, nm	E_g, eV	*n*@632.8 nm
Zn_1Mg_0O	8.1	-	166 ± 8	24 ± 8	4 ± 2	159	3.23 ± 0.07	1.81 ± 0.08
$Zn_{0.74}Mg_{0.26}O$	3.6	14.5 ± 0.7	208 ± 2	-	13 ± 1	-	3.80 ± 0.03	1.88 ± 0.01
$Zn_{0.56}Mg_{0.44}O$	6.4	-	209 ± 2	-	29 ± 1	-	3.72 ± 0.35	1.83 ± 0.01
$Zn_{0.51}Mg_{0.49}O$	8.2	7.2 ± 0.1	140 ± 1	-	13 ± 1	-	4.18 ± 0.10	1.80 ± 0.02
$Zn_{0.34}Mg_{0.66}O$	5.9	-	281 ± 4[1)]	5.8 ±0.7	34 ± 1	277	4.32 ± 0.03 (3.19 ± 0.15)	1.75 ± 0.05 1.84 ± 0.05

[1)] The total thickness of the film consisting of two layers, where the 1st layer is 75 nm thin, and the 2nd layer is 206 nm thin.

MSE - mean square error of the model, d_{int} - thickness of the interphase, *d* - thickness of the film *d* (roughness excluded), d_{NU} (%) - thickness non-uniformity, d_s (nm) - surface roughness, E_g - optical band gap, *n* - refractive index *n* at 632.8 nm. For comparison *d* obtained by TEM is given for some samples.

3.2. Optical absorption

Optical absorption of the WZ $Zn_{1-x}Mg_xO$ epilayers for x=0, 0.26, 0.44, 0.49, 0.66 was measured in the temperature range 10-300 K. Fig. 4 presents the results of the OA measurements at 10 K. For Zn_1Mg_0O sample, the absorption curve was typical for ZnO: in the near-band-gap region, it had characteristic exciton features around 3.4 eV, where two subbands were clearly seen. According to [28 references therein], depending on the sample treatment, up to three dominating subbands could be observed in the OA spectrum of ZnO, which were interpreted as free exciton transitions from the valence band to the conduction band. The valence band of ZnO

split into three subbands due to the influence of crystal field and spin-orbit interactions; hence, there are three free exciton transitions corresponding to each subband designated by symbols *A*, *B*, and *C*.

Other $Zn_{1-x}Mg_xO$ samples had OA spectra with band edge shifted to the higher energies, and the larger was MgO concentration, the larger was the shift of the band edge. The exciton absorption band for these samples was revealed as an unstructured bump on the band edge slope. Energy positions of the exciton absorption band, determined from the graphs for all samples, are shown in Table 2. Exciton absorption bands demonstrated the blue shift with an increase in MgO concentration. It should be mentioned that with the increase of MgO concentration, the band edge slope in the OA spectra became ever gentler. It could be explained by the increased structural inhomogeneity, providing a larger number of localized states, forming the Urbach tail. [37 Zhang]. The absorption curve of the $Zn_{0.34}Mg_{0.66}O$ had a minor feature at around 3.4 eV, corresponding to the free exciton absorption in pure ZnO. This observation corresponded to the ellipsometric studies of the sample, where SE analysis revealed inhomogeneity of the refractive index *n* in $Zn_{0.34}Mg_{0.66}O$. The first 75 nm of this film had *n* and E_g values comparable within the error with those of ZnO (Fig.2, Table 1), and the rest of the 260 nm film had the optical properties corresponding to ZnO-MgO compound.

The band gap values at 10 and 300 K were determined for all the studied $Zn_{1-x}Mg_xO$ samples, applying the Tauc plot to the absorption curves: $(\alpha h\nu)^2$ versus photon energy $h\nu$. The photon energy $h\nu$ and absorption coefficient α are linked to band gap energy E_g by relation [40 Rathore and references therein]:

$$\alpha h\nu = K\left(h\nu - E_g\right)^2, \quad (2)$$

where *K* is a constant. From the Tauc plot, the band gap value was determined as an intersection point of the tangent to a curve with an abscissa. Fig 5. shows the detection of a band gap value on the example of $Zn_{0.34}Mg_{0.66}O$ at low temperature, where two band gap values can be discriminated: one for ZnO-MgO compound (E_{g1}=4.35 eV), another for pure ZnO (E_{g2}=3.35 eV). All other $Zn_{1-x}Mg_xO$ samples had only one band gap, whose values varied from 3.35 eV for x=1 to 4.35 eV for x=0.34 at a temperature of 10 K. With temperature rise, the band gap energy decreased due to an increase of atomic vibrations leading to larger interatomic spacing and increased interaction of free charge carriers with lattice phonons [56, 57]. As a result, the band gap energies demonstrated the red shift. Band gaps of the studied $Zn_{1-x}Mg_xO$ epilayers determined using the Tauc plot at room temperature constituted values from 3.29 to 4.3 eV, correspondingly. All band gap values at 10 and 300 K are presented in Table 2.

Both SE and optical absorption experiments confirmed that the increase in MgO content caused the sequential blue shift of the $Zn_{1-x}Mg_xO$ band gap. That might be explained by the appearance of the larger number of electrons due to the lower electron affinity of MgO compared to ZnO, which occupied the energy levels located at the bottom of the conduction band. Electron transitions between the top of the valence band and unoccupied states of the conduction band, rising ever higher with an Mg increase, would increase the energy of the lowest optical transitions, thus contributing to the increase of the band gap [52, 54].

3.3. Photoluminescence

Photoluminescence spectra of WZ ZnMgO thin films were measured in the 10-300 K temperature region; the normalized spectra of all samples at 10 K are shown in Fig.6. PL spectra of all $Zn_{1-x}Mg_xO$ samples are presented with a near band edge (NBE) narrow band and a broad green defect band. Just as the band gap, NBE luminescence bands are consistently shifted to higher energies with an increase in MgO concentration in ZnMgO alloys. Thus, NBE emission peaks at 10 K are located at 3.33, 3.76, 3.93, 4.09 and 4.25 eV for x=0, 0.26, 0.44, 0.49 and 0.66.

Generally, the NBE luminescence band in ZnO relates to free and bound excitons [28 Ozgur]. In PL spectra of high-quality ZnO samples, a complicated structure of NBE emission is observed. The 3.37 – 3.55 eV region contains several features corresponding to transitions of free excitons from the conduction band to three valence subbands. *A*-free-exciton binding energy of 60 meV determines the Stokes shift compared to the absorption band. The 3.348 – 3.374 eV region of PL spectra is determined by the presence of several bound excitons, which are localized near neutral or charged donors and acceptors. The most intense is a line at 3.3605 eV assigned to *A* excitons, which are bound to neutral donors. In the 3.1- 3.3 eV region of the PL spectrum, the fine structure is determined by LO phonon replicas of the main exciton transitions.

In the NBE emission bands of the samples under investigation, no fine structure features could be distinguished even at the lowest temperatures, mainly because of the small thickness of samples, providing relatively low PL signal, and equipment resolution limitations. At low temperatures, the dominant contribution in NBE emission was provided by the bound excitons. That followed from correspondence of the Zn_1Mg_0O exciton band's maximum (3.327 eV) to the region of the bound excitons [28] and peculiarities of the thermal evolution of NBE luminescence in $Zn_{1-x}Mg_xO$, which will be described further.

The full width at half-maximum (FWHM) of NBE emission bands of samples could be estimated from the PL spectra in Fig. 6. The FWHM value was the smallest for Zn_1Mg_0O: at temperature10 K, it was 115 meV; for $Zn_{74}Mg_{26}O$, it became larger– 205 meV, and for the epilayers, with the high MgO content, it became ever larger– around 300-330 meV. FWHM values at 10 K are found in Table 2. An increase of FWHM in $Zn_{1-x}Mg_xO$ epilayers with growing x corresponds to literature data [38, 44, 58] and can be explained by chemical inhomogeneity and strain due to random alloying or Mg clustering, increasing with MgO concentration, which provides a number of slightly differing exciton states resulting in broadening of the emission peaks.

It is also worth mentioning that some of the PL spectra in Fig. 6 exhibited strong emission in the blue to red regions due to the presence of deep-level radiative defects. The deep level emission (DLE) of the Zn_1Mg_0O sample possessed a maximum intensity of approximately2.8 eV, which was higher than the value of 2.3 eV of the MBE grown ZnO epilayer reported in literature [59]. The broad DLE peak at 2.7 eV could be caused by either recombination of conduction band electrons with holes trapped at shallow acceptors or recombination of electrons trapped on shallow donors to holes at the valance band. The shallow donor and acceptor states could be related to Zn interstitial (Zn_i) and Zn vacancy (V_{Zn}) defects, respectively. The former was

located about 0.3-0.4 eV below the bottom of the conduction band, whereas the latter had energy distributed in a range from 0.2 to 0.9 eV [60-65]. Emission bands in the 2.4 - 2.1 eV energy region might relate to electron transitions between the defect levels linked to oxygen vacancies (V_O, V_O^{1+}, V_O^{2+}) and the valence band [8]. However, the intensity of the DLE peak in the $Zn_{74}Mg_{26}O$ spectrum was significantly reduced at the addition of Mg to 0.26, probably due to the strong inhibition effect of Mg on the formation of Zn_i proposed by Li et al. [66]. In addition, the DLE peak was observed again at energy of 2.9 eV and 3.2 eV for the $Zn_{56}Mg_{44}O$ and $Zn_{34}Mg_{66}O$ samples, respectively. Qui et al. [67] pointed out the possibility that Mg atoms might occupy the interstitial sites in ZnO as the Mg content exceeded far beyond the thermodynamic solubility limits. The emission peak corresponding to the recombination of trapped electrons from Mg_i to holes at the valence band was reported to exhibit energy of 3.0 eV or above [60], which was very close to those of the DLE peaks for the two samples. The presence of vacancy and interstitial defects in the studied $Zn_{1-x}Mg_xO$ compounds was determined by the growth conditions of the particular samples. Similar low-energy emission bands showing chaotic behaviour both in intensity and energy were also observed in other ZnMgO compounds [34].

Fig.7 demonstrates the absorption and emission spectra for the investigated $Zn_{1-x}Mg_xO$ samples. Here the position of exciton bands attracts the main interest. The observed Stokes shift, calculated as the difference between exciton absorption (indicated by arrows) and emission energies, constituted around 50 meV for x=0, 290 meV for x=0.26, and remained within the value of 600 meV for higher MgO concentrations. The dependence of Stokes shift on Mg concentration might be explained by potential fluctuations of the band gap caused by spatially inhomogeneous alloy composition. Random alloying or the creation of Mg clusters could generate microscopic potential minima, causing exciton transitions with lower energy [68].

3.4. Thermal behaviour of Photoluminescence

Some characteristic features of the material may be determined from PL dependence on temperature. With temperature rise, the PL intensity of both exciton and defect bands decreased in the studied $Zn_{1-x}Mg_xO$ samples, and the energy position of the exciton band shifted. Typical PL behaviour with temperature rise from 10 to 300 K is shown in Fig. 8 on an example of $Zn_{0.56}Mg_{0.44}O$. Other $Zn_{1-x}Mg_xO$ samples demonstrated similar thermal evolution of PL.

The decrease of the exciton luminescence intensity with temperature (temperature-dependent emission quenching) is determined by an increased rate of the nonradiative recombination process. The transition from radiative to non-radiative process is characterized by nonradiative thermal activation energy E_a, which is interpreted as thermal energy necessary for the liberation of the bound exciton from the localization of the potential minimum. Activation energy can be found from the Mott-Seitz equation [69],

$$I(T) = \frac{I_0}{1+a\cdot exp(-\frac{E_a}{kT})} \quad (3)$$

where I_0 and $I(T)$ are luminescence intensities at temperatures 0 and T, k is Boltzmann constant, and a is a frequency factor, determined by the ratio of radiative τ_R and nonradiative lifetimes τ_{NR}: $a=\tau_R/\tau_{NR}$.

In the Arrhenius plot, the activation energy is characterized by the slope of the linear part of the curve at higher temperatures. Arrhenius plot of exciton luminescence is shown in Fig. 9 for all the samples under investigation. From Fig.9, it is seen that the slopes of the Arrhenius curves obtained for the studied samples differed only slightly from each other and demonstrated no correspondence to the MgO content. For Zn_1Mg_0O, the estimated E_a value constituted 36 meV, which was larger than the values reported in the literature - 15 meV [37, 38]. Activation energies of other $Zn_{1-x}Mg_xO$ samples were found to be in the 46-90 meV range, irrespective of the concentration range of MgO. This differed from the regularity observed in [38], where activation energy increased sequentially from 15 meV to 127 meV for x= 0…0.37 in WZ $Zn_{1-x}Mg_xO$ compounds grown on *c*-plane sapphire substrates. The inconsistency in activation energy values in the present study those reported in literature could be explained by the structural properties of the samples under investigation, producing microscopic potential minima with different energy depths, depending on both random Mg alloying and on compound production conditions.

Another important characteristic of the exciton band is the dependence of its position on temperature. The behaviour of the exciton band energy at temperature growth, both in pure ZnO and in $Zn_{1-x}Mg_xO$ epilayers, can show either continuous red shift [38] or S-type dependence (red shift – blue shift – red shift). In the case of ZnO, the S-type behaviour of the maximum position was explained by the thermal evolution of bound and free excitons [28, 70]. According to these authors, at the lowest temperatures, the exciton peak resulted from recombination luminescence of a bound exciton, which showed a red shift with temperature rise due to the narrowing of the band gap. At $T \geq 65$ K, a free exciton band with the higher energy emerged at the expense of the thermal release of bound excitons and became a dominating feature at around $T \geq 175$ K, thus providing a blue shift. At ever higher temperatures, the free exciton band obeyed the thermal shrinkage of the band gap.

In the case of ZnO-MgO compounds, the exciton band was ascribed to bound excitons throughout the temperature region up to RT. Then the observed S-type behaviour of the exciton band was explained by the presence of the bound excitons localized in alloy-induced potential fluctuations [37, 38]. The rise of temperature stimulated the overcoming of the shallower potential barriers and recombination of bound excitons with a red shift. With the further increase of temperature, the excitons were localized at the deeper potential fluctuation minima, providing a blue shift. At ever further increase of temperature, the recombination energy of bound excitons obeyed the thermal shrinkage of the band gap, thus demonstrating a red shift. Some authors reported the continuous red shift instead of the S-type behaviour of the exciton band in ZnO-MgO pseudobinary compounds [71].

The energy position of exciton luminescence maximum for the studied $Zn_{1-x}Mg_xO$ epilayers is shown in Fig. 10. The exciton bands showed a continuous red shift for all studied compound samples. No S-type behaviour of the exciton emission band was observed in the studied samples. The most probable reason for the continuous decrease of the exciton recombination energy was the presence of the bound excitons localized at compositional fluctuations of ZnO-MgO alloys throughout the used temperature region. Due to the difference in electron affinity and ionic radius of Mg^{2+} and Zn^{2+} ions, the increased number of Mg ions substituting for Zn ions in the ZnMgO lattice increased the number of defects, which acted as localization sites for

excitons, thus stimulating abundance and thermal stability of bound excitons. The relatively large values of activation energy mentioned above spoke in favour of exciton localization in deep potential fluctuations already at the lowest temperatures; their thermal release with following radiative recombination corresponded to narrowing of the band gap. The effect of insufficient sensitivity of the equipment used also could not be omitted.

Table 2. Energy parameters (eV) of the studied WZ $Zn_{1-x}Mg_xO$ epilayers.

$Zn_{1-x}Mg_xO$ sample	@ 300 K		@10K					
	SE E_g	OA E_g ± 0.01	OA E_g ± 0.01	Exciton abs. ± 0.01	Exciton PL ±0.005	Stokes shift ± 0.01	FWHM± 0.005	E_a ± 0.005
Zn_1Mg_0O	3.23 ± 0.07	3.29	3.35	3.38	3.334	0.05	0.115	0.036
$Zn_{0.74}Mg_{0.26}O$	3.80 ± 0.03	3.82	3.84	4.05	3.763	0.29	0.205	0.068
$Zn_{0.56}Mg_{0.44}O$	3.72 ± 0.35	4.02	4.05	4.53	3.932	0.60	0.330	0.046
$Zn_{0.51}Mg_{0.49}O$	4.18 ± 0.10	4.20	4.23	4.67	4.074	0.60	0.320	0.088
$Zn_{0.34}Mg_{0.66}O$	4.32 ± 0.03 (3.19 ± 0.15)	4.30; (3.29)	4.35; (3.35)	4.83	4.243	0.59	0.295	0.056

SE E_g and OA E_g band gap energy retrieved from SE and absorption measurements, Exciton abs and Exciton PL - exciton absorption and photoluminescence bands energy positions, Stokes shift as the difference of exciton absorption and emission energies, FWHM – full width at half maximum of exciton emission band, E_a - nonradiative thermal activation energy.

The used methods of SE, OA and PL had provided mutually complementary results, which allowed comprehensive characterization of particular thin film samples, including energy parameters determined by sample composition, as well as the presence of chemical phases and interphases, layer thickness and roughness induced by peculiarities of the epitaxy process. Summarizing the results of optical spectroscopy studies of WZ $Zn_{1-x}Mg_xO$ epilayers, we noticed that samples grown by the plasma-assisted molecular beam epitaxy on SCAM substrate with an increase of MgO content revealed the sequential blue shift of the band gap width; free exciton absorption energy, and bound exciton emission energy (see Table 2). The main interest was attracted by the band gap values because this parameter determined the applicability of WZ $Zn_{1-x}Mg_xO$ epilayers for the UV sensors. It is noteworthy that E_g values of the studied materials, obtained by methods of SE and OA, were very close and constituted numbers from 3.23 eV to 4.32 eV at RT and from 3.35 eV to 4.35 eV at 10 K (x = 0,…, 0.66), shown in Fig.11. The only diverged point in the dependence was that obtained by SE for $Zn_{0.59}Mg_{0.44}O$: 3.72 ± 0.35 eV. The diminished band gap value was explained by the reduced sensitivity of the SE method due to very small oscillations of (Ψ, Δ) related to similar optical constants between SCAM and this thin film. However, within the error limits, this E_g value matched with E_g obtained from OA: 4.02 ± 0.01 eV.

For comparison, the data from other literature sources are also shown in Fig.11. Band gap values obtained from transmission measurements of WZ ZnO-MgO thin films [44] practically coincided with the results of the present investigation. Data from [72] and the lower part (at x < 0.3) of the curve from [73] related to WZ type $Zn_{1-x}Mg_xO$ also were in good correspondence with the present results. On the contrary, the data from [72] for (x > 0.3) and those from [34, 74] related to the RS type $Zn_{1-x}Mg_xO$ were

characterized by the distinguished behaviour of the band gap dependence versus Mg content. The graph demonstrates that compared to the previous studies, the samples under the present investigation maintain the WZ structure up to higher Mg values (x = 0.66).

The Urbach tail of the fundamental absorption edge also demonstrated a sequential increase with the rise of MgO concentration. Other spectral parameters of WZ $Zn_{1-x}Mg_xO$ thin films, such as Stokes shift and FWHM of exciton luminescence, showed the smallest values for x=0, larger ones for x=0.26, and approximately equal values for x=0.44, 0.49, 0.66. The thermal quenching activation energy was obtained as 36 meV for Zn_1Mg_0O and 56-88 meV for the $Zn_{1-x}Mg_xO$ epilayers. An increase of MgO content in the studied materials caused ever-growing structural inhomogeneity or composition fluctuations, which had generated slightly differing energy states, causing an increase of Urbach tail, Stokes shift, FWHM of exciton emission band and thermal nonradiative activation energy. Some of these parameters did not follow the MgO concentration sequentially within the whole studied range (x = 0, …, 0.66), that could be explained by particular conditions of sample production, providing an individual set of uncontrolled structural defects. As an example, the sample $Zn_{0.34}Mg_{0.66}O$ could be mentioned, which, apart from the alloy layer ZnO-MgO, had a layer of amorphous ZnO, revealed in SE and OA measurements. Moreover, thin interphase layers (with optical properties similar to ZnO) were also found in the $Zn_{0.74}Mg_{0.26}O$ and $Zn_{0.51}Mg_{0.49}O$ samples.

A perfect candidate for deep UV sensor material should have an absorption spectrum with a steep band edge in the UV region without any features in the visible spectral region. Though the values of the band gap of the studied WZ $Zn_{1-x}Mg_xO$ epilayers were appropriate for this purpose, the shape of the optical cut-off was not steep, especially for higher MgO concentrations. It was explained with growth of Urbach tail due to increased number of inhomogeneity-induced localization states with increase of MgO concentration. Besides, the presence of the defect band in the visible region of the absorption spectrum observed in all studied samples was not favourable for material application for UV sensors. In general, the WZ $Zn_{1-x}Mg_xO$ thin films grown on SCAM substrate by plasma-assisted molecular beam epitaxy have demonstrated a tuned band gap in the UV region and could be recommended for application as UV light sensor materials, provided that some corrections in the production process were implemented to control the quality of the film structure to eliminate the structural imperfections.

Conclusions

Spectroscopic ellipsometry, optical absorption, and photoluminescence methods were applied to determine optical, luminescence properties, and film quality values (e.g., surface roughness, thickness non-uniformity, optical gradient) of wurtzite $Zn_{1-x}Mg_xO$ epilayers (x=0, 0.26, 0.44, 0.49, 0.66) grown by the plasma-assisted molecular beam epitaxy on $ScAlMgO_4$ substrate. The results of the investigation have shown that an increase of MgO content in the $Zn_{1-x}Mg_xO$ compounds caused the blue shift of the band gap up to 4.35 eV at 10 K (4.32 eV at RT), an increase in exciton absorption and emission energy, and the blue shift of refractive index and extinction coefficient peak positions. The decrease of refractive index from 1.88 to 1.75 at low photon energies was observed for $Zn_{1-x}Mg_xO$ epilayers with an increase of x from 0.26 to 0.49. The character of the thermal evolution of PL of $Zn_{1-x}Mg_xO$ compounds allowed

assignment of the band edge emission to the luminescence of bound excitons. The increased values of Stokes shift and FWHM of exciton emission, thermal quenching activation energy, and Urbach tail in the absorption spectrum, were determined by the increased number of inhomogeneity-induced localization states with rising of MgO concentration.

The WZ $Zn_{1-x}Mg_xO$ thin films grown on SCAM substrate by plasma-assisted molecular beam epitaxy demonstrated a tuned band gap in the UV region and could be recommended for application as UV light sensor materials, provided that some corrections in the production process were implemented to control the quality of the film structure in order to eliminate the structural imperfections demonstrated by the spectroscopic analysis.

Acknowledgements
The financial support of the M-ERA.NET project "ZnMgO materials with tunable band gap for solar-blind UV sensors" (ZMOMUVS) is greatly acknowledged. Institute of Solid State Physics, University of Latvia, as the Center of Excellence, has received funding from the European Union's Horizon 2020 Framework Program H2020-WIDESPREAD-01-2016-2017-TeamingPhase2 under Grant Agreement No. 739508, project CAMART^2.

References

1. I. Ayoub, V. Kumar, R. Abolhassani, R. Sehgal, V. Sharma, R. Sehgal, H. C. Swart, Y.K. Mishra, Advances in ZnO: Manipulation of defects for enhancing their technological potentials. Nanotechnol. Rev. 11 (2022) 575 – 6191.

2. C. Li, C. Han,Y. Zhang, Z. Zang, M.Wang, X. Tang, J. Du, Enhanced photoresponse of self-powered perovskite photodetector based on ZnO nanoparticles decorated $CsPbBr_3$ films. Solar Energy Materials and Solar Cells. 172 (2017) 341-346.

3.Y. Guo, Y. Zhang, T. Li, T.J. Tao, ZnO quantum dots for fluorescent detection of environmental contaminants. Environ. Chem. Eng. 9 (2021) 106800.

4. E. K. Droepenu, B. S. Wee, S. F. Chin, K. Y. Kok, M. F. Maligan, Zinc oxide nanoparticles synthesis methods and its effect on morphology: A review. Biointerface Research in Applied Chem. 12 (2022) 4261 – 429215.

5. V. García-Salcido, P. Mercado-Oliva, J. L. Guzmán-Mar, B. I. Kharisov, L. Hinojosa-Reyes, MOF-based composites for visible-light-driven heterogeneous photocatalysis: Synthesis, characterization and environmental application studies. J. Solid State Chem. 307 (2022) 122801.

6. M. M. Ahmed, R. Zhao, J. Du, J. Li, Review - Nanostructural ZnO-Based Electrochemical Sensor for Environmental Application. J. Electrochem. Soc. 169, (2022) 020573.

7. F. H. Abdullah, N. H. H. A. Bakar, M. A. Bakar, Current advancements on the fabrication, modification, and industrial application of zinc oxide as photocatalyst in the removal of organic and inorganic contaminants in aquatic systems. J. Hazard. Mater.42415 (2022) 127416.

8. H. B. Cuong, N. M. Le, S.- H. Jeong, B. - T. Lee, Tailoring of composition, band-gap, and structural phase in ZnMgO films by simply controlling growth temperature and oxygen partial pressure during sputter deposition. J. Alloys Compd. 30 (2017) 54-63.

9. Q. Li, W. Zeng, Y. Li, Metal oxide gas sensors for detecting NO_2 in industrial exhaust gas: Recent developments. Sens. Actuators B: Chem. 35915 (2022) 131579.

10. H. Wang, H. Li, W. Cai, P. Zhang, S.Cao, Z.Chen, Z. Zang, Challenges and strategies relating to device function layers and their integration toward high-performance inorganic perovskite solar cells. Nanoscale 12 (2020) 14369-14404.

11. S. Sulaiman, S. Izman, M. B. Uday, M. F. Omar, Review on grain size effects on thermal conductivity in ZnO thermoelectric materials. RSC Advances12 (2022) 5428 – 543831.

12. K. Magiswaran, M.N. Norizan, I.S. Mohamad, N. Mahmed, S.N. Idris, S.A. Sobri, Charge Recombination in Zinc Oxide-Based Dye-Sensitized Solar Cell: A Mini Review. Int. J. Nanoelectro. Mater. 14, (2021), 59 – 66.

13. P. Dhiman, G. Rana, A. Kumar, G. Sharma, D.-V. N. Vo, M. Naushad, ZnO-based heterostructures as photocatalysts for hydrogen generation and depollution: a review. Environ.Chem. Lett.(2022) doi: 10.1007/s10311-021-01361-1.

14. Z. Zang, Efficiency enhancement of ZnO/Cu_2O solar cells with well oriented and micrometer grain sized Cu_2O films. Appl. Phys. Lett. 112, 042106 (2018).

15. C. Gutiérrez Rodelo, R.A. Salinas, E. Armenta Jaime, S. Armenta, A. Galdámez-Martínez, S.E. Castillo-Blum, H. Astudillo-de la Vega, A. Nirmala Grace, C.A. Aguilar-Salinas, J. Gutiérrez Rodelo, G. Christie, W.F. Alsanie, Zinc associated nanomaterials and their intervention in emerging respiratory viruses: Journey to the field of biomedicine and biomaterials. Coord. Chem. Rev. 45715 (2022) 214402.

16. I. S. Okeke, K. K. Agwu, A. A. Ubachukwu, F. I. Ezema, Influence of transition metal doping on physiochemical and antibacterial properties of ZnO Nanoparticles: A review. Appl. Surf. Sci. Adv. 8 (2022) 100227.

17. E. Cojocari, O. Ignatov, M. Jian, V Cobzac., T. Braniște, E.V. Monaico, A. Taran, V. Nacu, Zinc Oxide and Gallium Nitride Nanoparticles Application in Biomedicine: A Review. IFMBE Proc. 87, (2022) 373 – 381.

18. J. Rodrigues, S. O. Pereira, J. Zanoni, C. Rodrigues, M. Brás, F.M. Costa, T. Monteiro, ZnO Transducers for Photoluminescence-Based Biosensors: A Review. Chemosensors 10 (2022) 39.

19. F. Sharifianjazi, A. Jafari Rad, A., Bakhtiari, F. Niazvand, A. Esmaeilkhanian, L. Bazli, M. Abniki, Biosensors and nanotechnology for cancer diagnosis (lung and bronchus, breast, prostate, and colon): A systematic review. Biomed. Mater. (Bristol) 17 (2022) 012002.

20. Manikandan S., Subbaiya R., Saravanan M., Ponraj M., Selvam M., Pugazhendhi A., A critical review of advanced nanotechnology and hybrid membrane based water recycling, reuse, and wastewater treatment processes.Chemosphere 289 (2022) 132867.

21.S Ghosh, A. Malloum, C. A. Igwegbe, J. O. Ighalo, S. Ahmadi, M. H. Dehghani, A. Othmani, Ö. Gökkuş, N. M. Mubarak, New generation adsorbents for the removal of fluoride from water and wastewater: A review. J. Mol. Liq. 34615 (2022) 118257.

22. X. Yang, M.Hu,T. Su, X. Ma,Y. Chen, X. Kong, W. Ren, Volume-matched ferroelectric and piezoelectric ZnO/MgO superlattice. J. Alloys Compd. 876 (2021) 160167.

23. K. Ferri, S. Bachu, W. Zhu, M.Imperatore, J.Hayden, N.Alem, N.Giebink, S. Troiler-McKinstry, J.-P. Maria, Ferroelectrics everywhere: Ferroelectricity in magnesium substituted zinc oxide thin films.J. Appl. Phys. 130 (2021) 044101.

24. L. Meng, Z. Lv, H. Chai, X. Yang and T. Yang, A-axis oriented $Zn_{0.72}Mg_{0.28}O$ epitaxial thin films with large second-order nonlinear susceptibility.J. Phys. D: Appl. Phys., 55(19) (2022) 19LT01.

25. J. A. Spencer, A. L. Mock, A. G. Jacobs, M. Schubert, Y. Zhang, M. J. Tadjer, A review of band structure and material properties of transparent conducting and semiconducting oxides: Ga_2O_3, Al_2O_3, In_2O_3, ZnO, SnO_2, CdO, NiO, CuO, and Sc_2O_3.Appl. Phys. Rev. 9 (2022) 011315.

26. L. Chu, C. Xu, W. Zeng, C. Nie, Y. Hu, Fabrication and Application of Different Nanostructured ZnO in Ultraviolet Photodetectors: A Review. IEEE Sens. J. (2022) doi: 10.1109/JSEN.2022.3158650.

27. B. E. Sernelius, K.-F. Berggren, Z.-C. Jin, I. Hamberg and C. G. Granqvist Band-gap tailoring of Zno by means of heavy Al doping, Phys. Rev. B 37 (1988) 10244-10248.

28. U. Ozgur, Ya. I. Alilov, C. Lui, A. Teke, M. A. Reshchikov, S. Dogan, V. Avrutin, S.-J. Cho and H. Morkoc. A comprehensive review of ZnO materials and devices. J. Appl. Phys. 9 (2005) 041301.

29. Y. J. Lu, Z. Shi, C.-X. Shan, D- Z. Shen, ZnO-based deep-ultraviolet light-emitting devices. Chin. Phys. B 26(4) (2017) 047703.

30. T. Zhang, M. Li, J. Chen, Y. Wang, L. Miao, Y. Lu, Y. He, Multi-component ZnO alloys: Bandgap engineering, hetero-structures, and optoelectronic devices.Mater. Sci. .Eng. R: Rep.147 (2022) 100661.

31. C. Zhou, Q. Ai, X. Chen, X. Gao, K. Liu, D. Shen. Ultraviolet photodetectors based on wide bandgap oxide semiconductor films. Chin. Phys. B . 28 (2019) 048503.

32. A. Djelal, K. Chaibi, N. Tairi, K. Zitouni, A. Kadri. Ab-initio DFT-FP-LAPW/TB-mBJ/LDA-GGA investigation of structural and electronic properties of $Mg_xZn_{1-x}O$ alloys in wurtzite, rocksalt and zinc-blend phases. Superlattices Microstruct. 109 (2017) 81-88.

33.P. Dluzevski, J. Domagala, S. Kret, D. Jarosz, M. Krysko, H. Teisseyre, Phase – transition critical thickness of rocksalt $Mg_xZn_{1-x}O$ layers. J.Chem. Phys. 154 (2021) 154701.

34. I. Gorczyca, M. Wierzbowska, D. Jarosz, J. Z. Domagala, A. Reszka, D. Le Si Dang, F. Donatini, N. E. Christensen and H. Teisseyre, Rocksalt ZnMgO alloys for ultraviolet applications: Origin of band-gap fluctuations and direct-indirect transitions, Phys. Rev. B 101, 245202 (2020), 13 p.

35.Y. Hou, Z. Mei, X. Du, Semiconductor ultraviolet photodetectors based on ZnO and $Mg_xZn_{1-x}O$. J.Phys. D: Appl. Phys. 47 (2014) 283001.

36. C. Xie, X.-T. Lu, X.-W. Tong, Z.-X. Zhang, F.-X. Liang, L. Liang, L.-B. Luo, Y.-C. Wu. Recent progress in solar-blind deep-ultraviolet photodetectors based on inorganic ultrawide bandgap semiconductors. Adv. Func. Mater. (2019) 1806006.

37. J. Zhang, W. Tian, F. Wu, S. Sun, S. Wang, J. Dai, Y. Fang, Z. Wu, C. Chen, J. Tai, M. Li, Y. He. Optical properties of the nonpolar a-plane MgZnO films grown on a-GaN/r-sapphire templates by pulsed laser deposition. Opt. Mat. Express 4 (2014) 2346-2354.

38. T. Wassner, B. Laumer, S. Maler, A. Laufer, B. Meyer, M. Stutzmann and M. Eickhoff. Optical properties and structural characteristics of ZnMgO grown by plasma assisted molecular beam epitaxy. J. Appl. Phys. 105 (2009) 023505.

39. C. Xu, X. Pan, H. He, Z.Ye, Excitation-intensity and temperature dependences of photoluminescence in ZnMgO film. J. Lumin. 226 (2020) 117456.

40. D. Rathore, S. Arora. Investigation and optical properties of $(ZnO)_x$-$(MgO)_{1-x}$ (x=1.0,0.75, 0.50, 0.20, 0.10) nano crystalline thin films. Materials Today: Proceedings 30 (2020) 164-167.

41. Tao Yan, L. Trinkler, V. Korsaks, C.-Y.J. Lu, B. Berzina, L. Chang. M. M. C. Chou and K. H. Ploog, Anisotropic photoluminescence of nonpolar ZnO epilayers and ZnO/$Zn_{1-x}Mg_xO$ multiple quantum wells grown on $LiGaO_2$ substrate. Opt. Express 28 (2020) 5629-5638.

42. R. Kara, S. Rachid, A. Azizi, Effect of i-ZnO seed layer on the properties of electrodeposited p-Cu_2O/n-ZnO/FTO heterojunction thin films Mater. Res. Express, 6 (12) (2019) 126402.

43. M. C. Wen, S. A. Lu, L. Chang, M. M. C. Chou, K. H. Ploog. Epitaxial growth of rocksalt $Zn_{1-x}Mg_xO$ on MgO (100) by molecular beam epitaxy. J. Cryst. Growth 477 (2017) 169-173.

44. M. C. Wen, T. Yan, L. Chang, M. M. C. Chou, N. Ye, K. H. Ploog. Achieving high MgO content in wurtzite ZnO epilayer grown on $ScAlMgO_4$ substrate. J. Cryst. Growth. 477 (2017) 174-178.

45. A. S. Ferlauto, G. M. Ferreira, J.M. Pearce, C.R. Wronski, R.W. Collins, X. Deng, G. Ganguly, Analytical model for the optical functions of amorphous semiconductors from the near-infrared to ultraviolet: Applications in thin film photovoltaics. J. Appl. Phys. 92 (2002) 2424-2436.

45. X. Liang, H.-Q. Wang, L.Zhang, K. Kisslinger, J. Kang, Interface and optical properties of $Zn_{1-x}Mg_xO$ films with Mg content of more than 70% grown on the (1 10)-ZnO substrates. AIP Advances 11, (2021) 075217.

46. D. E. Aspnes, J. Theeten, and F. Hottier, Investigation of effective-medium models of microscopic surface roughness by spectroscopic ellipsometry. Phys. Rev. B 20, 3292 (1979)

47. L. A. Pettersson, L. Hultman, and H. Arwin, Porosity depth profiling of thin porous silicon layers by use of variable-angle spectroscopic ellipsometry: a porosity graded-layer model. Appl. Opt. 37, 4130-4136 (1998).

48. H. Arwin, Physical Is ellipsometry suitable for sensor applications? Sens. Actuators A, 92 (2001) 892, 43-51.

49. M. Zubkins, J. Gabrusenoks, G. Chikvaidze, I. Aulika, J. Butikova, R. Kalendarev, L. Bikse, Amorphous ultra-wide bandgap ZnO_x thin films deposited at cryogenic temperatures, J. Appl. Phys. 128 (2020) 215303

50. A. Dejneka, I. Aulika, M. V. Makarova, Z. Hubicka, A. Churpita, D. Chvostova, L. Jastrabik, and V. A. Trepakov, Optical Spectra and Direct Optical Transitions in Amorphous and Crystalline ZnO Thin Films and Powders, J. Electrochem. Soc. 157 (2010) G67.

51. Z. K. Heiba and L. Arda, Structural properties of $Zn_{1-x}Mg_xO$ nanomaterials prepared by sol-gel method, Cryst. Res. Technol. 44(8) (2009) 845.

52. A. Kaushal and D. Kaur, Effect of Mg content on structural, electrical and optical properties of $Zn_{1-x}Mg_xO$ nanocomposite thin films. Sol. Energy Mater. Sol. Cells 93(2) (2009) 193.

53. C. Teng, J. Muth, Ü. Özgür, M. Bergmann, H. Everitt, A. Sharma, C. Jin, J. Narayan, Refractive indices and absorption coefficients of $Mg_xZn_{1-x}O$ alloys, APL 76(8) (2000) 979.

54. N. Ouarab, M. Boumaoura, First-principles calculations of electronic and optical properties of $Fe_{1-x}Zn_xS_2$ and $Zn_{1-x}Mg_xO$ alloys, Curr Appl Phys 17(9) (2017) 1169.

55. S. Lindroos, M. Leskelä, Growth of zinc peroxide (ZnO_2) and zinc oxide (ZnO) thin films by the successive ionic layer adsorption and reaction–SILAR–technique, Int. j. inorg. 2(2-3) (2000) 197-201.

56. Y. P. Varshni, Temperature dependence of the energy gap in semiconductors, Physica, 34 (1967) 149-154.

57. K. P. O'Donnell and X. Chen, Temperature dependence of semiconductor band gaps. Appl.Phys.Lett. 58 (1991) 2924-2926.

58. E. Mosquera, J. E. Diosa, Luminescence of ZnO/MgO phosphors, Optik 243 (2021) 16716.

59. A1. D. M. Hofmann, D. Pfisterer, J. Sann, B. K. Meyer, R. Tena-Zaera, V. Munoz-Sanjose, T. Frank and G. Pensl, Properties of the oxygen vacancy in ZnO. Appl. Phys. A 88 (2007) 147-151.

60. A2. M. Trunk, V. Venkatachalapathy, A. Galeckas, A. Yu. Kuznetsov. Deep level related photoluminescence in ZnMgO. Appl. Phys. Lett. 97, 211901 (2010);

61. A3. A. Janotti and C. G. Van de Walle, Fundamentals of zinc oxide as a semiconductor. Rep. Prog. Phys. 72 (2009) 126501.

62. A4. S. A. M. Lima, F. A. Sigoli, M. Jafelicci, and M. R. Davolos, Luminescent properties and lattice defects correlation on zinc oxide. Int. J. Inorg. Mater. 3 (2001) 749.

63. A5. E. G. Bylander, Surface effects on the low-energy cathodoluminescence of zinc oxide. J. Appl. Phys. 49 (1978) 1188.

64. A6. C. H. Ahn, Y. Y. Kim, D. C. Kim, S. K. Mohanta, and H. K. Cho, A comparative analysis of deep level emission in ZnO layers deposited by various methods. J. Appl. Phys. 105 (2009) 013502.

65. A7. J. Hu and B. C. Pan, Electronic structures of defects in ZnO: Hybrid density functional studies. J. Chem. Phys. 129 (2008) 154706.

66. A8. W Li, L Fang, G Qin, H Ruan, H Zhang, Tunable zinc interstitial related defects in ZnMgO and ZnCdO films. J. Appl. Phys. 117 (2015) 145301.

67. A9. X. Qiu, L. Li, J. Zheng, J. Liu, X. Sun, Origin of the Enhanced Photocatalytic Activities of Semiconductors: A Case Study of ZnO Doped with Mg^{2+}. J. Phys. Chem. C 112 (2008) 12242-12248.

68. M. D. Neumann, C. Cobet, N. Esser, B. Laumer, T. A. Wassner, M. Eickhoff, M. Feneberg, and R. Goldhahn, Optical properties of MgZnO alloys: Excitons and exciton-phonon complexes. J. Appl.Physics 110 (2011) 013520.

69. S. W. S. McKeever. Thermoluminescence of Solids. Cambridge University Press, 1988.

70. T. Makino, N. T. Tuan, H. D. Sun, C. U. Chia, Y. Segawa, M. Kawasaki, A. Ohtomo, K.Tamura, T. Suemoto, H. Akiyama, M. Baba, S. Saito, T. Tomila, H. Koinuma. Temperature dependence of near ultraviolet photoluminescence in ZnO/(Mg, Zn)O multiple quantum wells. Appl. Phys. Lett. 78 (2001) 1979-1981.

71. T. Makino, K. Tamura, C. H. Chia, Y. Segawa, M. Kawasaki, A. Ohtomo and H. Koinuma. Temperature quenching of exciton luminescence intensity inZnO/(Mg,Zn)O multiple quantum wells. J. Appl. Phys. 93 (2003) 5929-5933.

72.A. Ohtomo, M. Kawasaki, T. Koida, K. Masubuchi, H. Koinuma, Y. Sakurai, Y. Y osida, T. Yasuda, Y. Segawa, $Mg_xZn_{1-x}O$ as a II–VI widegap semiconductor alloy. Appl. Phys. Lett., 72 (1998), pp. 2466-2468.

73. X. Wang, K. Saito, T. Tanaka, M. Nishio, Q. Guo, Lower temperature growth of single phase MgZnO films in all Mg content range. J. Alloys Compd. 627 (2015) 383-387.

74. S. Choopun, R.D. Vispute, W. Yang, R.P. Sharma, T. Venkatesan, H. Shen, Realization of band gap above 5.0 eV in metastable cubic-phase $Mg_xZn_{1-x}O$ alloy films. Appl. Phys. Lett., 80 (2002), pp. 1529-1531.

Figure captions

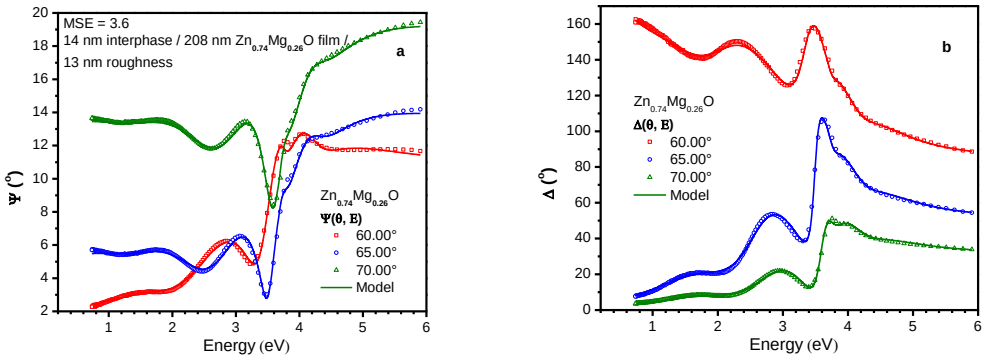

Figure 1. Experimental (symbols) and modelled (line) main ellipsometric angles Ψ (a) and Δ (b) vs photon energy at three angles θ for the $Zn_{0.74}Mg_{0.26}O$ thin film.

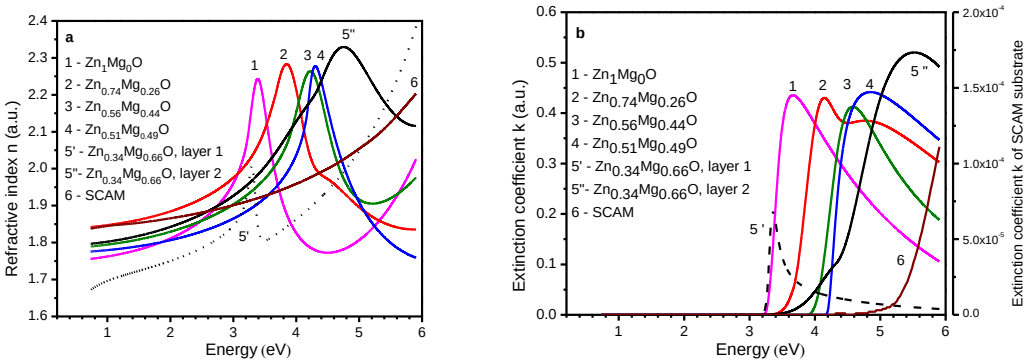

Figure 2. Refractive index *n* (a) and extinction coefficient *k* (b) dispersion curves of SCAM substrate and five $Zn_{1-x}Mg_xO$ compounds. The sample $Zn_{0.34}Mg_{0.66}O$ was modelled as two-layer thin film (see layer 1 (5') and layer 2 (5") *n* and *k* curves). The given *n* curves of $Zn_{0.34}Mg_{0.66}O$ are mean values of the *n* near the surface and near the bottom for the layers 1 and 2.

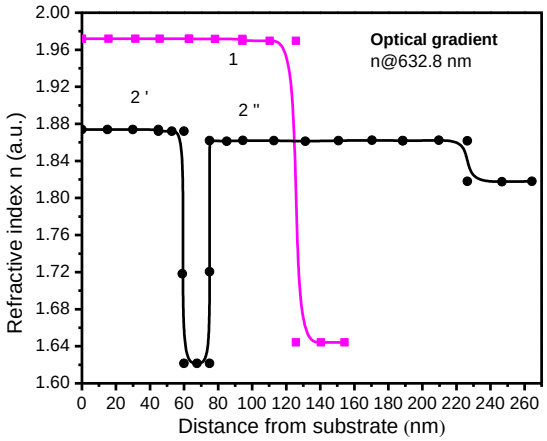

Figure 3. The change of refractive index at 632.8 nm for ZnO (1) and $Zn_{0.34}Mg_{0.66}O$ epilayers. The $Zn_{0.34}Mg_{0.66}O$ was modelled as two-layer thin film, where the first layer (2') was is 75 nm thin, and the second layer (2'') - 206 nm thin.

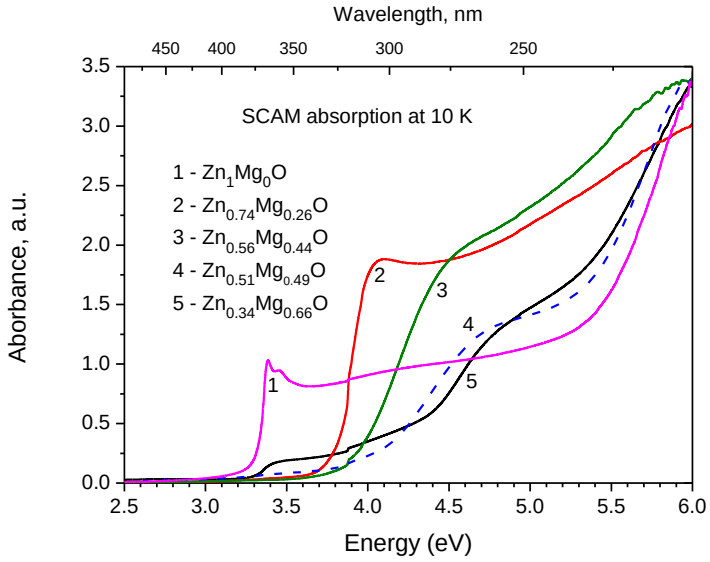

Figure 4. Optical absorption of WZ ZnMgO thin films at 10 K.

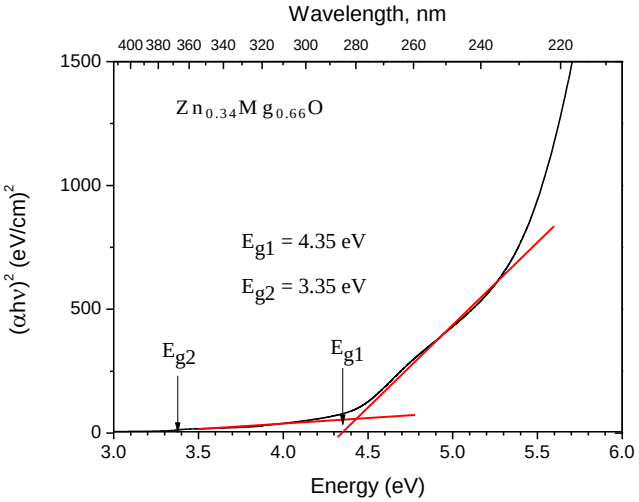

Figure 5. Tauc plot for $Zn_{0.34}Mg_{0.66}O$ at temperature 10 K.

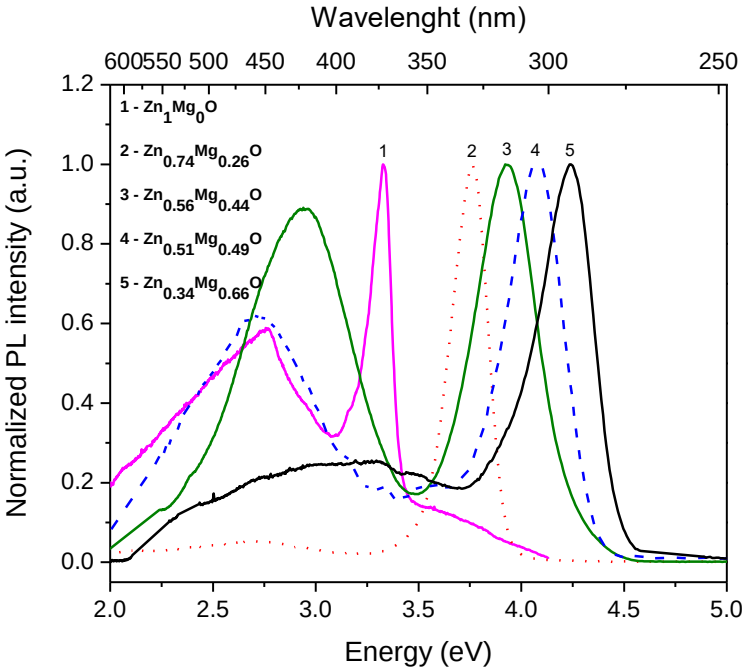

Figure 6. Normalized photoluminescence spectra of WZ $Zn_{1-x}Mg_xO$ thin films at temperature 10 K excited with wavelengths 290 nm (1) and 260 nm (2-5).

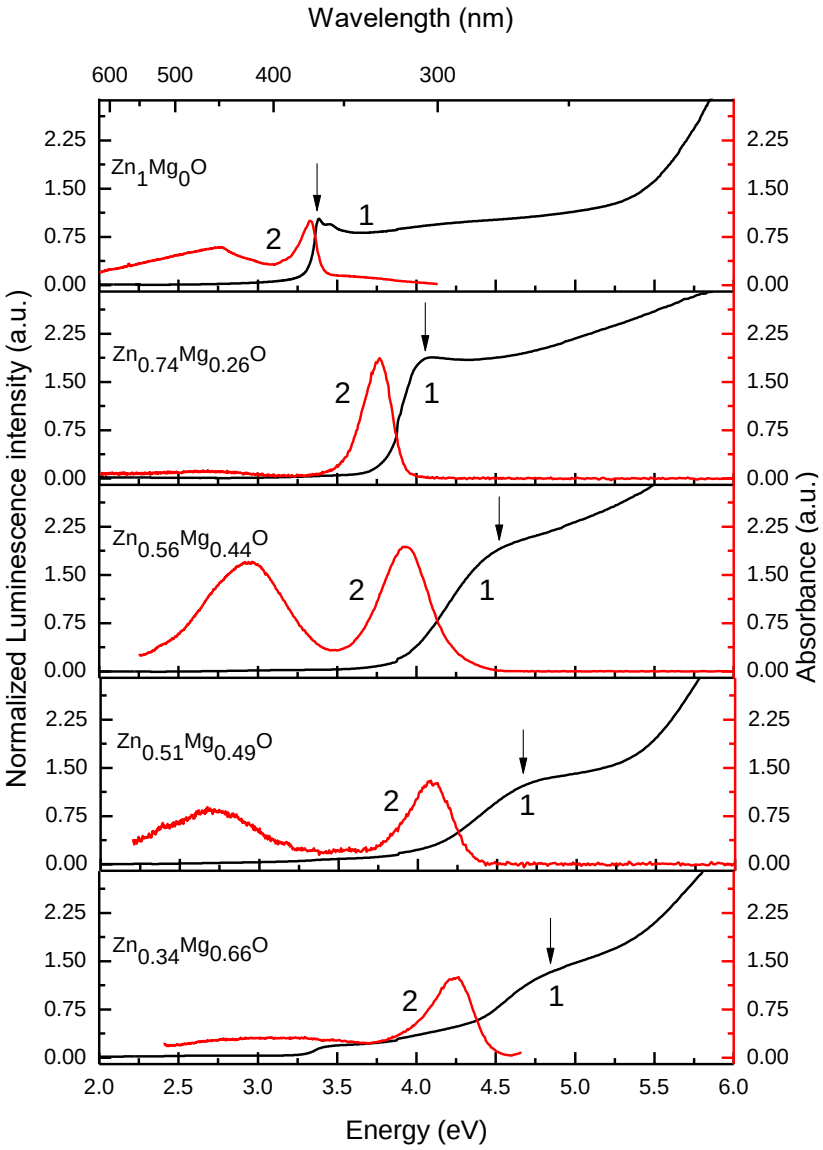

Figure 7. Comparison of absorption (1) and PL (2) spectra, demonstrating Stokes shift of exciton bands for $Zn_{1-x}Mg_xO$ alloys at temperature 10 K. Arrows indicate position of exciton absorption energy.

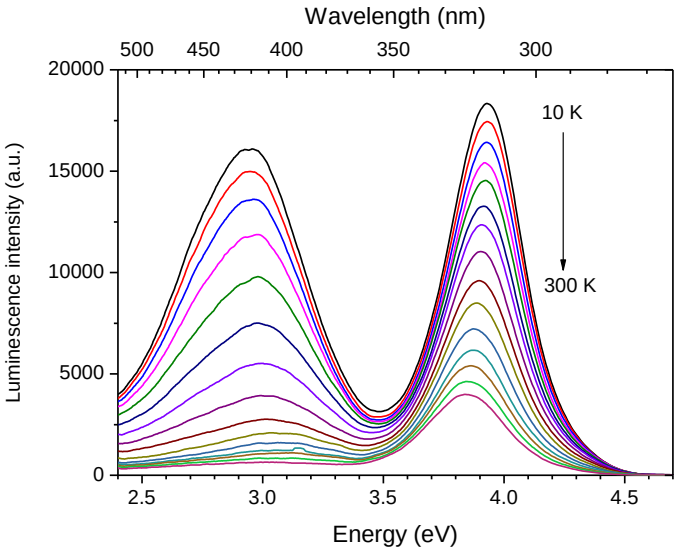

Figure 8. PL spectra of $Zn_{0.56}Mg_{0.44}O$ in the 10-300 K temperature range under excitation 260 nm.

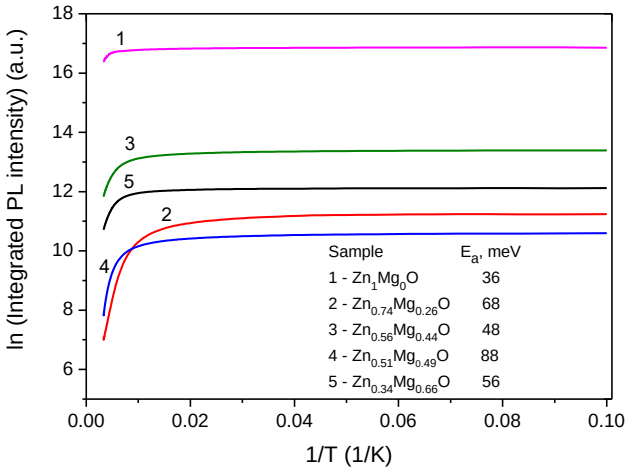

Figure 9. Arrhenius plot of integrated PL intensity of exciton luminescence band in the studied WZ $Zn_{1-x}Mg_xO$ epilayers. Calculated activation energies of the samples are shown in the legend.

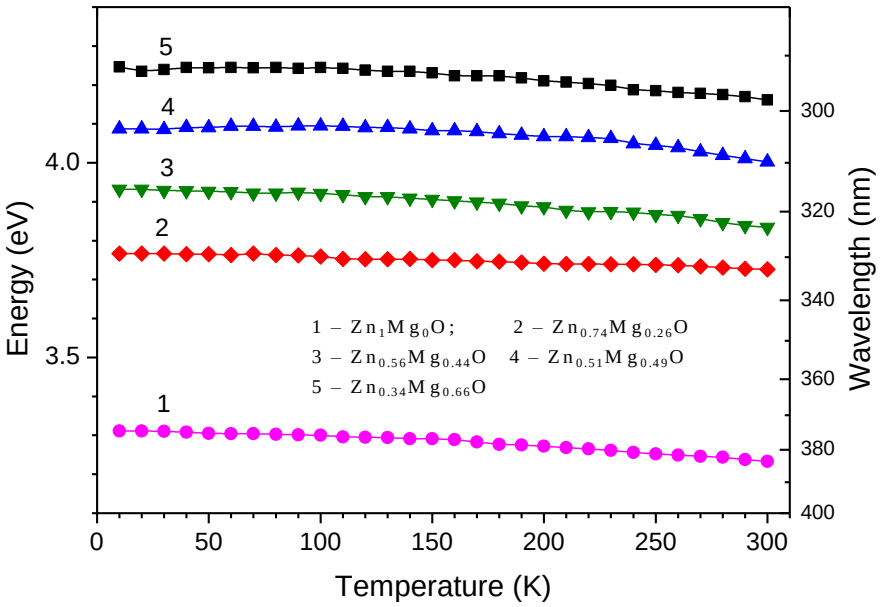

Figure 10. Thermal evolution of exciton emission band peak for $Zn_{1-x}Mg_xO$ epilayers.

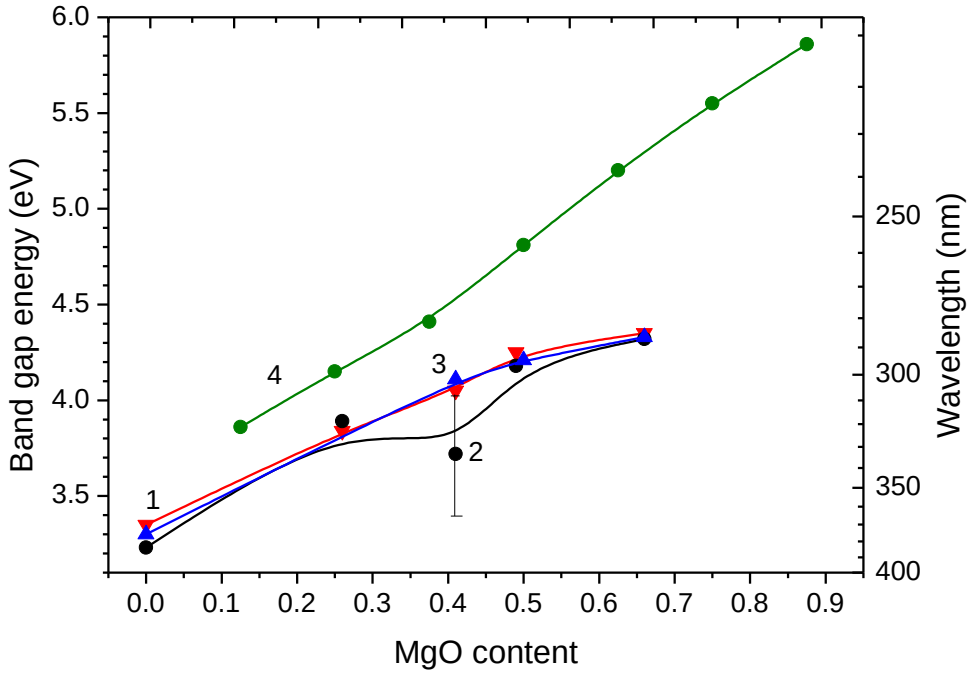

Figure 11. $Zn_{1-x}Mg_xO$ band gap energy dependence on Mg content: obtained from OA at 10 K and SE at RT in the present study (an error bar is shown for E_g of $Zn_{0.56}Mg_{0.44}O$, obtained by SE); obtained from transmittance measurements at RT [44, 72-74], and CL at RT [34].